research papers

Tris-amidoximate uranyl complexes *via* η^2 binding mode coordinated in aqueous solution shown by X-ray absorption spectroscopy and density functional theory methods

Linjuan Zhang,[a]* Meiying Qie,[a] Jing Su,[a] Shuo Zhang,[a] Jing Zhou,[a] Jiong Li,[a] Yu Wang,[a] Shitong Yang,[b] Shuao Wang,[b] Jingye Li,[a] Guozhong Wu[a] and Jian-Qiang Wang[a]*

[a]Shanghai Institute of Applied Physics, Chinese Academy of Sciences, Shanghai 201800, People's Republic of China, and [b]School for Radiological and Interdisciplinary Sciences (RAD-X), Soochow University, Suzhou 215123, People's Republic of China. *Correspondence e-mail: zhanglinjuan@sinap.ac.cn, wangjianqiang@sinap.ac.cn

The present study sheds some light on the long-standing debate concerning the coordination properties between uranyl ions and the amidoxime ligand, which is a key ingredient for achieving efficient extraction of uranium. Using X-ray absorption fine structure combined with theoretical simulation methods, the binding mode and bonding nature of a uranyl–amidoxime complex in aqueous solution were determined for the first time. The results show that in a highly concentrated amidoxime solution the preferred binding mode between UO_2^{2+} and the amidoxime ligand is η^2 coordination with tris-amidoximate species. In such a uranyl–amidoxime complex with η^2 binding motif, strong covalent interaction and orbital hybridization between U $5f/6d$ and (N, O) $2p$ should be responsible for the excellent binding ability of the amidoximate ligand to uranyl. The study was performed directly in aqueous solution to avoid the possible binding mode differences caused by crystallization of a single-crystal sample. This work also is an example of the simultaneous study of local structure and electronic structure in solution systems using combined diagnostic tools.

1. Introduction

Extracting uranium from seawater, which contains ∼4.5 billion tons of U (Davies *et al.*, 1964), is an effective way to meet the increasing demand for nuclear fuel as advanced nuclear energy systems continue to develop. Extraction using adsorbent materials is a promising method for sequestering considerably low concentrations of uranium in seawater. Over 200 functionalized polymers exist as adsorbents; among them, the amidoxime-functionalized polymers are highly selective towards uranium (Schenk *et al.*, 1982; Astheimer *et al.*, 1983; Seko *et al.*, 2004; Kim *et al.*, 2013; Witte *et al.*, 1984; Das *et al.*, 2009; Ting *et al.*, 2013; Vukovic & Hay, 2013) and have achieved capacities as high as 3.3 g uranium kg^{-1} adsorbent (Kim *et al.*, 2014). Despite more than three decades of investigation, the only insight into how the amidoxime ligand binds to the uranyl ions in an aqueous environment has been accomplished mainly through computational investigations. In aqueous solution, the absence of long-range ordering rules out the diffraction method, while other typical spectroscopies such as IR provide limited structural information. Raman spectra can give useful information for investigating the molecules and chemical bonding in solution (Liu *et al.*, 2017; McGrail *et al.*, 2014), but cannot determine the local coordination struc-

ture. The identification of the coordination environment of the uranyl complex is critical, especially in aqueous solution, to understand the uranium extraction mechanism from seawater and even design an organic functionalized adsorbent under non-equilibrium conditions.
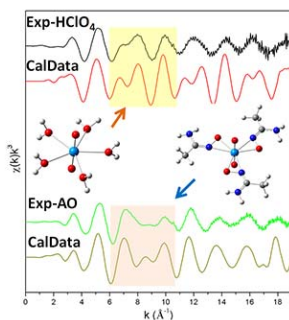
The coordination mode between amidoxime and UO_2^{2+} has been studied extensively, and three possible binding motifs have been reported as shown in Fig. 1. Witte firstly observed a monodentate oxygen-binding mode in a uranyl–amidoxime crystal (Fig. 1a), in which uranium is bound to the oxygen atoms of two amidoxime and two amidoximate ligands (Witte *et al.*, 1984). Zhang and Katragadda suggested a chelating interaction (Fig. 1b) (Zhang *et al.*, 2005; Katragadda *et al.*, 1997), illustrating that U coordinates the oxygen atom of NOH and the nitrogen atom of NH_2, but until now no representative single crystal has been reported. The η^2 binding motif, which corresponds to the uranium bound to the oxygen and nitrogen atoms of the amidoxime ligand, was recently predicted to be the most stable structure on the basis of density functional theory (DFT) calculations and crystallography (Fig. 1c) (Barber *et al.*, 2012; Vukovic *et al.*, 2012; Guo, Wang *et al.*, 2015; Wang *et al.*, 2014). Using the available studies, several issues must be noted. First, most of the recent studies were based on the DFT method and direct experimental evidence remains relatively rare. The few existing experimental data were obtained through single-crystal X-ray structural analysis in non-aqueous media. Second, theoretical calculation is helpful in exploring the coordination structure of uranyl complexes in an aqueous environment. Almost all prior theoretical reports predicted that the η^2 binding motif is thermodynamically preferred in aqueous media (Vukovic *et al.*, 2012; Guo, Wang *et al.*, 2015; Wang *et al.*, 2014); however, a five-coordinate 1:2 uranyl complex with mixed coordination of two ligands is reported to be more stable than a pure η^2 binding motif after applying a correction of the coupled cluster theory with simple, double and perturbative triple excitations [CCSD(T)] (Abney *et al.*, 2016). Shi and his colleague also reported monodentate and η^2 coordination are the main binding modes for the amidoxime group in the presence of carbonate ligand (Wang *et al.*, 2014). Third, the recent experimental results are mainly based on a single-crystal phase in a non-aqueous environment, where the single-crystal structure may be affected by many factors, such as the

preparation conditions and the solvent medium. However, the structures obtained in non-aqueous media, although highly informative, are less relevant to the uranyl complexes in aqueous solution. The coordination structure of uranyl complexes can be affected by the concentration and temperature of the solution (Bailey *et al.*, 2005; Gückel *et al.*, 2013; Hennig *et al.*, 2007). In aqueous solution, the participation of OH^- or H_2O has a great impact on the coordination configurations of uranyl (Neuefeind *et al.*, 2004). Puckered-hexagon configurations of OH^- or H_2O about the uranyl group will tend to revert to plane-pentagon coordination (Evans, 1963). Additional water molecules can cause the change from bidentate to monodentate modes due to different proton transfer and thus lead to different electronic properties (Jackson *et al.*, 2013). The relative complexation ability of ligands and water determines the uranyl species when strongly coordinating ions are present, and water may even be excluded entirely from the first coordination sphere. Thus, direct experimental determination of the coordination structure of uranyl complexes in the aqueous environment is essential. Unfortunately, the local structure in solution is difficult to obtain and thus there is great demand for an experimental technique combining an element-specific probe technique and accurate analysis. X-ray absorption spectroscopy is such a tool, and has been successfully applied in exploring the coordination structure in a solution.

The present work accurately investigated the coordination property of a UO_2^{2+}–amidoxime complex in aqueous solution through X-ray absorption fine structure (XAFS) along with DFT calculations. Considering the extremely low U concentration in seawater, in the local space of the uranyl extraction process the dose of amidoxime is relatively high and thus the present research was performed in a highly concentrated amidoxime system. As a comparison, the uranyl–$HClO_4$ solution was considered, which is believed to be pure hydrate complexes due to the weak coordinating ability of perchlorate ions (Sémon *et al.*, 2001). Combined with the theoretical simulation, quantitative XAFS analysis is a powerful tool to investigate the local structural information. In this combined diagnostic method, DFT calculations were performed to optimize and identify the possible spatial arrangement from various binding motifs, as inputs for extended X-ray absorption fine structure (EXAFS) simulations. The corresponding theoretical spectrum that optimally matches the experimental pattern reflects the real spatial arrangement of the uranyl–amidoxime complex in solution. This work was directly performed in a solution to avoid the possible variations in binding mode caused by the crystallization process of a single-crystal sample.

2. Experimental and theoretical investigation

All samples were prepared from $UO_2(NO_3)_2 \cdot 6H_2O$, which was dissolved in aqueous solutions containing the required concentration of $HClO_4$ or $CH_3C(NH_2)(NOH)$ (referred to as AO). In the sample, the concentrations of U and $HClO_4$ were maintained at 0.04 M and 1 M, respectively, and the AO
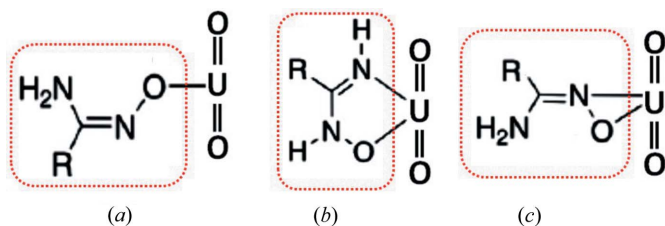

Figure 1
Three possible binding motifs between the amidoxime ligand and UO_2^{2+} cation. (a) Monodentate binding to the oxygen atom of the oxime ligand, (b) bidentate chelation involving the oxime oxygen atom and amide nitrogen atom, and (c) η^2 binding with the N—O bond.

concentration was adjusted to 5 M. This choice of ion concentration was based on previous work (Ikeda-Ohno et al., 2009). The 5 M AO concentration was chosen to ensure the excess of AO ligands relative to the uranyl ions, which is similar to the local environment in the extraction of uranium.

The uranium L_3-edge XAFS spectra were collected at beamline 14W1 of the Shanghai Synchrotron Radiation Facility with a Si (111) double-crystal monochromator in transmission mode. The electron beam energy of the storage ring was 3.5 GeV and the maximum stored current was ~210 mA. The energy calibration was performed using a Zr foil (~17 998 eV). Each sample was measured thrice and the obtained spectra were averaged. The U L_3-edge XAFS data were analysed by the Demeter program (Ravel & Newville, 2005). The double-electron excitations affect the EXAFS signal and can influence the results of data analysis (see Fig. S1 in the supporting information) (Hennig, 2007; Benfield et al., 1994; Gomilšek et al., 2003; Kodre et al., 2002; Zhang, Zhou et al., 2016). Thus, in uranium L_3-edge EXAFS experimental spectra the double-electron excitations were subtracted as a reflection of the data translated to the position in energy of the excitation using the standard procedures in Demeter. Fig. S1 shows the uranium L_3-edge EXAFS data before and after subtracting the double-electron excitation in k and R space, in which the feature at very short distances ($R \simeq 1$ Å) obviously improved. The theoretical phase and amplitude functions were calculated using FEFF 9.0 (Rehr et al., 2010). Fitting was performed on the k^3-weighted FT-EXAFS (FT = Fourier transform) from 3.4 to 18.4 Å^{-1}. An R window of 1–3 Å was used for the fitting. The amplitude reduction factor S_0^2 was fixed at 0.9 in EXAFS fits and the shifts in the threshold energy ΔE_0 were constrained to be the same value for all fitted shells.

All density functional calculations were performed using the B3LYP hybrid functional (Becke, 1988; Lee et al., 1988) implemented in the Gaussian09 program (Frisch et al., 2009), which is widely used and proven to be sufficiently accurate for extensive systems. The cc-PVDZ basis sets (Dunning, 1989) were adopted for hydrogen, carbon, nitrogen and oxygen atoms. The reliability of our theoretical methods in predicting the structural parameters was also evaluated by optimizing the geometrical structures of the hydrated uranyl ions at the B3LYP/cc-PVDZ level of theory, in which the predicted bond lengths in the aqueous solution are considerably close to the experimental results. Geometry optimizations were performed without symmetry restrictions. Frequency calculations were also performed to verify the structures at the energy minima. Solvation effects were taken into account using the conductor-like polarizable continuum model (CPCM) (Klamt & Schüürmann, 1993; Barone & Cossi, 1998; Cossi et al., 2003; Andzelm et al., 1995). Natural population analyses (NPA) and Wiberg bond indices were calculated to understand the bonding of uranyl–AO complexes based on the B3LYP results through the natural bond orbital (NBO) method (Weinhold & Landis, 2005) implemented in the NBO 3.1 program (Glendening et al., 2003). Charge decomposition analysis (CDA) developed by Franking et al. (Dapprich & Frenking, 1995;

Frenking & Fröhlich, 2000) was performed as implemented in the Multiwfn 3.3 software (Lu & Chen, 2012).

3. Results and discussion

3.1. Uranium L_3-edge X-ray absorption near-edge structure (XANES) and EXAFS features of uranyl ions in HClO$_4$ and amidoxime solutions

The quantitative local structural information can be extracted by EXAFS analysis in R space, as shown in Fig. 2 and Table 1. The coordination polyhedron of the uranyl complex can be described as a bipyramid with the axial trans-dioxo atoms in the apical position and the equatorial coordination changed from tetragonal to hexagonal geometry. According to path analysis in R space, the peaks at R values of about 1.5 Å (A) and 2.0 Å (B) corresponded to the single scattering paths of the axial oxygen atoms (O$_{ax}$) and the equatorial ligands (L$_{eq}$), respectively. The fitting results revealed that the uranyl–HClO$_4$ solution contains a uranyl unit exhibiting an R(U—O$_{ax}$) of 1.77 Å and possesses five coordinated oxygen atoms derived from the water molecules at 2.41 Å along the equatorial plane. This result is consistent with the structure previously reported for hydrated uranyl ions (Neuefeind et al., 2004; Hennig et al., 2007; Sémon et al., 2001). By contrast, the distance of U—O$_{ax}$ (1.81 Å) in uranyl–AO solution is obviously longer than that in HClO$_4$ solution, which indicates that the AO molecule has stronger interaction than the water molecule with the uranyl ions, thus affecting the relative positions of the uranium and the axial oxygen atom. At first glance, the L$_{eq}$ shell of the uranyl–AO sample shows a splitting ($R + \Delta \simeq 1.7$ and 2.0 Å), similar to that of uranyl hydrate. However, previous investigations suggested that the FT peak ($R + \Delta = 1.7$ Å) originating from the superposition of the O$_{eq}$ shell with the side lobe of the O$_{ax}$ shell in uranyl–hydrate solution does not provide meaningful structural information (Ikeda-Ohno et al., 2008, 2009). A relative intensity reversal and position shift of the L$_{eq}$ shell are observed in the uranyl–AO sample compared with the hydrate. The stronger intensity at a peak of ~1.7 Å indicates that the peak is no longer attributed to the superposition of the L$_{eq}$ and O$_{ax}$ shells, but contains the real coordination structure. Considering the asymmetry of peak B, two possible U—L$_{eq}$ shells can be used; the fitting distances at 2.32–2.42 Å are shown in Table 1. The average bond length of U—L$_{eq}$ is about 2.37 Å. It is worth mentioning that EXAFS fits cannot differentiate between the coexisting atoms with close scattering ability, such as O and N atoms. Therefore, the result of the current EXAFS fitting is insufficient to provide insights into the spatial arrangement of the uranyl–AO complex.

As we know, the XANES feature is sensitive to the spatial structure. Fig. 3(a) shows the experimental L_3-edge XANES spectra of uranyl ions in HClO$_4$ and AO solutions, which are similar with both having a strong white line (WL) (A), a shoulder (B) at about 15 eV and a feature (C) at about 35 eV above the WL maximum. In terms of the scattering theory, the peaks in the spectrum could be ascribed to the backscattering

Table 1
EXAFS structural parameters of uranyl ions in $HClO_4$ and AO solutions.

O_{ax}, O_{eq} and L_{eq} represent the axial oxygen, equatorial oxygen and equatorial ligands in uranyl complexes, respectively. CN: coordination number.

Sample	Bond type	CN	R (Å)†	σ^2 (Å²)‡	R factor	Average distance of U−L_{eq}
UO_2^{2+} in	U−O_{ax}	2.0	1.77	0.0015	0.01	2.41 Å
1 M $HClO_4$	U−O_{eq}	5.0 ± 0.2	2.41	0.0058		
UO_2^{2+} in	U−O_{ax}	2.0	1.81	0.0015	0.01	2.37 Å
5 M AO	U−L_{eq1}	3.1 ± 0.3	2.32	0.0047		
	U−L_{eq2}	3.1 ± 0.3	2.42			

† Error: $R \leq \pm 0.02$ Å.   ‡ Debye–Waller factor. Error: $\sigma^2 \leq \pm 0.0005$ Å².
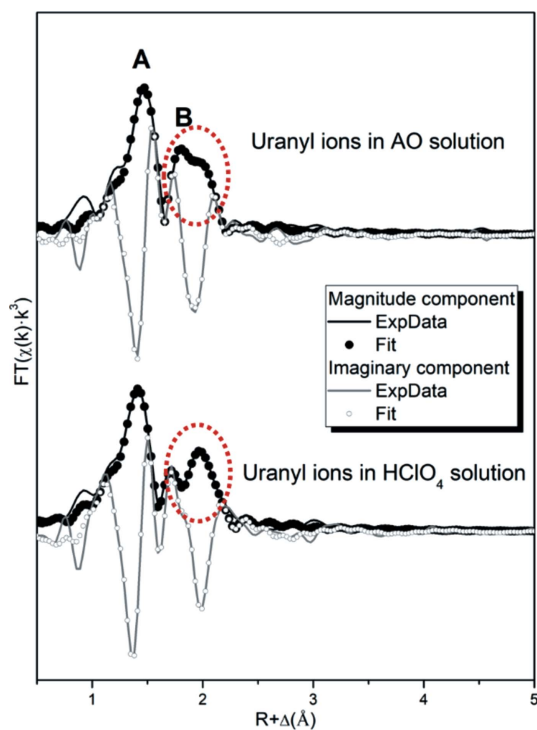

Figure 2
Magnitude and imaginary components of the Fourier transforms for the experimental data of the uranyl–$HClO_4$ and uranyl–amidoxime solutions as well as their corresponding fits.

of photoelectrons from different coordinated shells, and thus the intensity and shape of the peaks reveal the structure of the uranyl–AO complex. The most intense resonance A mainly originates from the dipole that allowed U $2p_{3/2} \rightarrow 6d$ electronic transitions. Two main observations are drawn from Fig. 3(a): (i) the line shapes in AO and $HClO_4$ solutions are consistent with each other, implying similarity in the coordination structure; (ii) the relative positions of peaks B and C slightly intensified in AO aqueous solution compared with those in $HClO_4$ environment. As previously mentioned (Sémon et al., 2001), in the perchlorate acid solution the uranyl ion is surrounded by pure hydrate molecules. By contrast, an obvious pattern improvement indicated that the existence of AO ligands can induce the adjustment of the local structural environment around the uranium atom. In fact, in the XANES spectra of uranyl compounds the energy positions of peaks B

and C depend on the U−O_{ax} and U−O_{eq} distances, respectively. Specifically, $1/R^2$ was proportional to ΔE, the difference between the multiple-scattering resonance and WL. Thus a shorter U−O_{ax} distance and a longer U−O_{eq} distance should be obtained in the $HClO_4$ solution than in the uranyl–AO solution, which is exactly consistent with the EXAFS analysis. Although very informative, the XANES analysis is too complicated to obtain the quantitative spatial structural information independently, especially for actinide chemistry.

To explore the spatial arrangement of the uranyl–AO complex, attention was paid to the EXAFS oscillation pattern. As we know, the EXAFS oscillation is a superimposition of individual scattering paths from ligand shell atoms; thus,
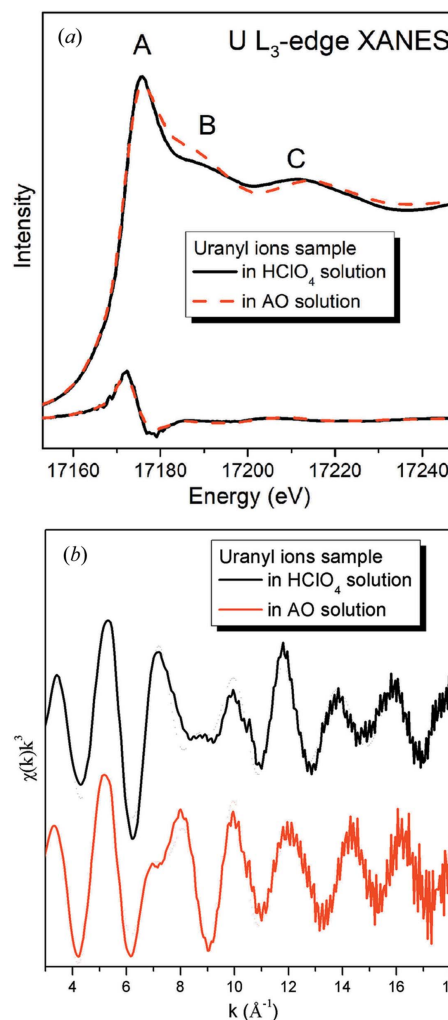

Figure 3
(a) Comparison between uranium L_3-edge XANES spectra of uranyl ions in $HClO_4$ (solid line) and AO (broken line) solutions. The bottom curves show the first derivative of XANES in two uranyl ion solutions. (b) Comparison between the uranium L_3-edge EXAFS oscillation pattern of uranyl ions in $HClO_4$ and AO solutions after subtracting the double-electron excitations.

Table 2
Optimized distances between uranium and ligand atoms, $R(U-O_{ax})$ (axial oxygen) and $R(U-L_{eq})$ (equatorial ligands), based on the CPCM DFT/B3LYP calculations of uranyl complexes.

The binding motifs are represented in Fig. 1: (*a*) monodentate binding to the oxygen atom of the oxime ligand, (*b*) bidentate chelation involving the oxime oxygen atom and amide nitrogen atom and (*c*) η^2 binding with the N−O bond. Values in bold: structural models exhibiting U−O$_{eq}$ distances of ∼2.34–2.40 Å, which are fairly close to the experimental value (2.37 Å).

Complexes	No.	Binding motifs/basis sets	R_{U-Oax} (Å)	R_{U-Leq} (Å)	Average R_{U-Leq} (Å)	CN
Hydrated species	0	cc-PVDZ	1.758, 1.758	2.420, 2.424, 2.426, 2.428, 2.477	2.435	5
		6-311G	1.758, 1.758	2.426, 2.426, 2.430, 2.439, 2.489	2.442	
		6-31+G(d,p)	1.760, 1.760	2.428, 2.429, 2.432, 2.441, 2.494	2.445	
		6-31++G*	1.760, 1.760	2.425, 2.428, 2.430, 2.438, 2.491	2.442	
Mono-AO species	**1**	**c**	**1.784, 1.784**	**2.247, 2.332, 2.454, 2.464, 2.464**	**2.392**	**5**
	2	b	1.782, 1.783	2.277, 2.472, 2.470, 2.481, 2.489	2.438	5
	3	a	1.788, 1.782	2.139, 2.524, 2.498, 2.514, 2.515	2.438	5
Di-AO species	**4**	**c/c**	**1.798, 1.798**	**2.292, 2.298, 2.417, 2.418, 2.538**	**2.392**	**5**
	5	b/b	1.799, 1.801	2.305, 2.326, 2.496, 2.525, 2.530	2.436	5
	6	a/a	1.798, 1.803	2.251, 2.257, 2.528, 2.530, 2.550	2.423	5
	7	c/b	1.798, 1.799	2.286, 2.304, 2.400, 2.514, 2.584	2.418	5
	8	**c/a**	**1.801, 1.803**	**2.242, 2.295, 2.382, 2.484, 2.522**	**2.385**	**5**
	9	b/a	1.799, 1.803	2.190, 2.349, 2.518, 2.546, 2.551	2.431	5
Tris-AO species	10	c/c/c	1.819, 1.820	2.330, 2.332, 2.332, 2.447, 2.447, 2.449	2.390	6
	11	**c/c/a**	**1.812, 1.818**	**2.208, 2.326, 2.334, 2.431, 2.445**	**2.349**	**5**
	12	b/b/b	1.817, 1.814	2.500, 2.550, 2.505, 2.540, 2.482, 2.551	2.521	6
	13	c/c/b	1.817, 1.817	2.342, 2.354, 2.415, 2.443, 2.451, 2.541	2.424	6
	14	c/b/b	1.816, 1.816	2.366, 2.433, 2.440, 2.466,, 2.538, 2.543	2.464	6
	15	**c/b/a**	**1.815, 1.811**	**2.208, 2.339, 2.387, 2.438, 2.553**	**2.385**	**5**
	16	b/b/a	1.812, 1.815	2.203, 2.390, 2.416, 2.546, 2.562	2.423	5

pattern changes directly reflect the local structure of the uranyl system. Fig. 3(*b*) shows the experimental EXAFS oscillation function for the U L_3 edge in *k* space with good quality up to $k = 19$ Å^{-1} in both HClO$_4$ and AO solutions. A couple of features are worth noting. First, the main EXAFS oscillation of the U L_3 edge becomes closer together in *k* space in the uranyl–AO complex, which originates from a longer U−O$_{ax}$ distance and has been verified by EXAFS fits in *R* space. Second, the EXAFS spectra of uranyl ions in the HClO$_4$ and AO solutions present markedly different characteristics, especially in the *k* range of 6–10 Å^{-1}. In order to clarify the origin of peak characteristic changes and obtain the spatial structure information, an assisted theoretical method is necessary.

3.2. Metal–ligand binding motif in the uranyl–AO solution

The possible isomeric structures of the uranyl–AO species in the aqueous solution were investigated by DFT calculations. DFT-optimized geometrical structures served as models and were used in EXAFS simulations. A comparison between the experimental spectra and the simulated EXAFS oscillation spectra may reveal the intrinsic coordinate structural information. To guarantee that the DFT-optimized structure is nearly similar to the experimental value, we first simulated the structure of the hydrated uranyl ions with typical basis sets for actinyl complexes such as 6-31++G*, 6-31+G(d,p) and 6-311G(d,p), as well as cc-PVDZ for oxygen and hydrogen atoms (Wang *et al.*, 2014; Dunning, 1989; Guo, Huang *et al.*, 2015; Di Santo *et al.*, 2011; Vetere *et al.*, 2003). Table 2 shows that the average bond length of U−O$_{ax}$/U−O$_{eq}$ (1.758 Å/2.435 Å) based on the cc-PVDZ basis sets is much closer to the experimental XAFS values ($R_{U-Oax} = 1.77$ Å, $R_{U-Oeq} =$

2.41 Å). We then used the same basis sets to optimize the structures of all possible uranyl–AO species. Table 2 shows the optimized structure of the possible $[UO_2(AO)_x]^{2-x}$ models, including the cationic compounds with mono-AO ligand, the neutral compounds with di-AO ligands and the anionic compounds with tris-AO ligands. The three possible binding motifs including monodentate, bidentate and η^2 modes were also considered. The DFT calculations revealed that the distances between uranium and the axial oxygen (U−O$_{ax}$) increased with the increase in AO coordination. The U−O$_{ax}$ distance in a uranyl complex with mono-AO ligand is 0.02 Å longer than that in the UO$_2$(OH$_2$)$_5^{2+}$ complex. Similarly, in uranyl complexes with tris-AO ligands the distances between U and the axial oxygen atoms are longer by 0.01–0.02 Å than those in complexes with two AO ligands and longer by 0.03–0.04 Å than those in mono-AO species. These results indicate that AO coordination weakens the U−O$_{ax}$ bonds considerably compared with water molecules. Observing the uranyl complex binding with the same number of AO ligands, different binding motifs have a negligible effect on the U−O$_{ax}$ distance, although obviously different characters of U−O$_{eq}$ bond length were observed, which may be attributed to varying binding strengths of the oxime oxygen atoms and oxime nitrogen atoms as well as of amide nitrogen atoms to uranyl ions (Wang *et al.*, 2014; Guo, Huang *et al.*, 2015). A comparison between the distances estimated by DFT and EXAFS assists in eliminating some of the proposed models with larger structural deviation. For example, most of the di-AO species exhibiting a bidentate chelation model involving the oxime oxygen atom and the amide nitrogen atom are rather unlikely because the U−O$_{eq}$ distances obtained by DFT are considerably longer compared with the values obtained by EXAFS fits (2.37 Å). All possible structural
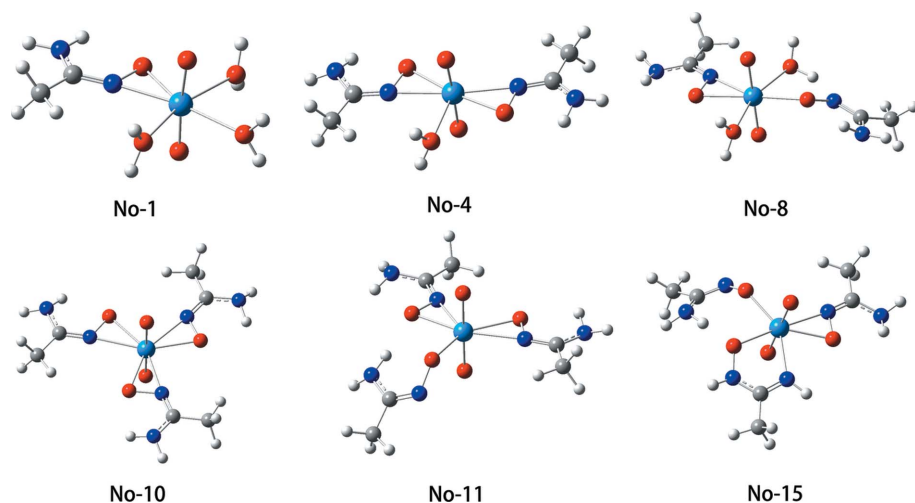
Figure 4
Optimized structures of the $[UO_2(AO)_x]^{2-x}$ complexes as a function of AO binding motif with U—O_{eq} distances of ~2.34–2.40 Å, which are fairly close to the experimental value (2.37 Å).

tural model. In Fig. 5(a), by carefully comparing the pattern between the experimental spectra and the simulated spectra of the optimized structures of the uranyl–AO species, we found that model No. 10 matched the experimental result very well, especially with regard to the appearance of an oscillation peak at approximately $k \simeq 8.5$ Å^{-1}. This result showed that the η^2 motif with tris-AO ligands is the main binding mode in the uranyl sample in solution containing high AO concentration. The corresponding theoretical XANES spectra of the No. 10 model are also similar to those of the experimental spectra as shown in Fig. 5(b). This binding motif is consistent with that of the previously reported crystal structure (Barber *et al.*, 2012; Vukovic *et al.*, 2012).

models exhibiting U—O_{eq} distances of ~2.34–2.40 Å, which are fairly close to the experimental value (2.37 Å), which are marked in bold in Table 2, and their corresponding geometries are displayed in Fig. 4.

To provide more direct evidence for determining the accurate binding mode, we calculated the corresponding EXAFS oscillation spectra based on the selected structural models optimized by DFT as shown in Fig. 4. Fig. 5(a) shows comparisons between the experimental and theoretical EXAFS spectra. For comparison, the pure hydration situation in the uranyl–HClO$_4$ complex is also displayed, in which the model with five water ligands was considered, and simulated theoretical spectra are shown in Fig. 5(a). A similar overall oscillation pattern in the experimental and theoretical case of HClO$_4$ solution can be observed particularly within 6–10 Å^{-1}, which again confirmed the reliability of the optimized struc-

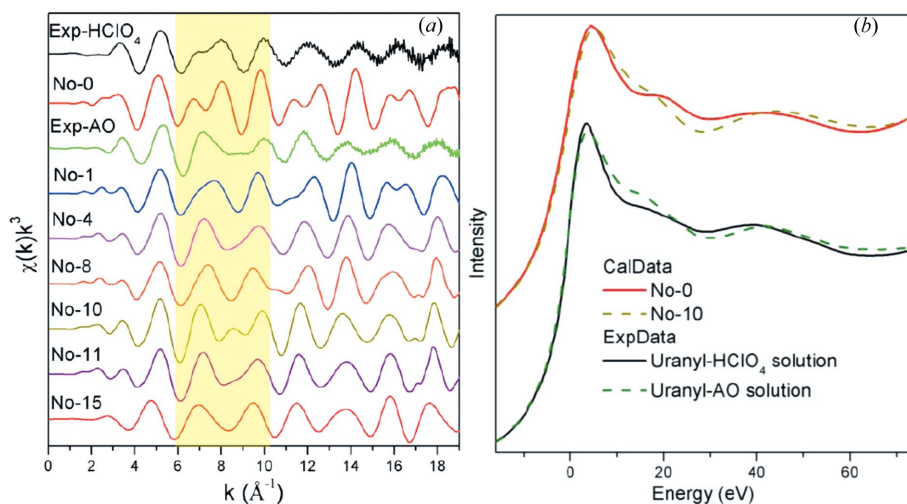### 3.3. Metal–ligand bonding nature in uranyl–AO complexes

The bonding nature including bond orders and atomic charges has been investigated through NBO analysis at the B3LYP level of theory for the uranyl–AO complexes with different binding motif and different AO number; results are summarized in Table 3. In all uranyl–AO complexes, the Wiberg bond indices (WBIs) of U—O_{AO}, U—N and U—O_w bonds show the following bond order trend: U—O_{AO} > U—N > U—O_w, indicating that the U—O/N bonds derived from the AO ligand have more covalent character than those from the H$_2$O molecule. The electron-donating ability of the ligands towards uranium can also be evaluated through NPA. Table 3 shows that the natural charges in the uranium atoms of these complexes are much lower than those of the free uranyl cations (2.736), demonstrating the significant charge transfer from the ligands to uranium (Wang *et al.*, 2014). As for the uranyl–AO complex with η^2 binding mode, the net charges on uranium atoms are lower than those in other complexes with monodentate or bidentate modes. This supports the larger electron-donating ability of the AO ligand to uranium in complex with η^2 binding mode. We also explore the bonding interaction in uranyl–AO complexes with different AO number. The WBIs of the U—O_{ax} bonds slightly decreased as the coordinated AO ligand increased, consistent with the slight increase in U—O_{ax} bond lengths in Table 2, which is well understood as equatorial orbital interaction slightly weakening the U—O triple bond in $[UO_2(AO)_x]^{2-x}$ ($x = 1$ to 3) complexes

Figure 5
(a) k^3-weighted experimental and calculated EXAFS oscillations of uranyl–AO species at the U L_3-edge, as well as the EXAFS pattern of the uranyl hydrate complex. (b) Experimental and simulated XANES spectra of uranyl–AO and uranyl–HClO$_4$ solutions.

Table 3
Wiberg bond indices (WBIs) of U—N and U—O bonds and natural charge analysis through DFT/B3LYP calculations.

Oxygen atoms in uranyl, water and AO ligand are labelled as O_{ax}, O_w and O_{AO}, respectively; ΔQ(AO/H_2O) indicates the change of natural charge from free AO/H_2O ligand to coordinated AO/H_2O ligand.

Compounds	WBIs				Natural charge		
	U—O_{ax}	U—O_w	U—O_{AO}	U—N	Q(U)	ΔQ(AO)	ΔQ(H_2O)
No3_Mono-motif [UO_2(AO)(H_2O)$_4$]$^+$	2.18	0.40	1.07		+1.50	+0.70	+0.21
No2_Bi-motif [UO_2(AO)(H_2O)$_3$]$^+$	2.19	0.44	0.84	0.57	+1.48	+0.85	+0.24
No1_η^2-motif [UO_2(AO)(H_2O)$_3$]$^+$	2.20	0.44	0.86	0.59	+1.44	+0.89	+0.24
No4_η^2-motif UO_2(AO)$_2$(H_2O)	2.14	0.36	0.75	0.49	+1.45	+0.74	+0.20
No10_η^2-motif UO_2(AO)$_3$$^-$	2.15		0.71	0.49	+0.95	+0.72	

HOMO-1,4%U5f$_{\delta\phi}$+86%O2p

Monodentate motif: No-3_[UO_2(AO)(H_2O)$_4$]$^+$

HOMO-3, 2%U5f$_\phi$+4%U6d$_\delta$+86%(N,O)2p
HOMO-1, 2%U5f$_\phi$+3%U6d$_\delta$+82%(N,O)2p

Bidentate chelation motif: No-2_[UO_2(AO)(H_2O)$_3$]$^+$

HOMO-1,7%U5f$_\phi$+7%U6d$_\delta$+74%(N,O)2p

η^2 motif: No-1_[UO_2(AO)(H_2O)$_3$]$^+$

HOMO-3,1%U5f$_\phi$+10%U6d$_\delta$+80%(N,O)2p
HOMO-2,12%U5f$_\phi$+75%(N,O)2p

η^2 motif: No-4_[UO_2(AO)$_2$(H_2O)]

HOMO-5, 14%U5f$_\phi$+84%(N,O)2p
HOMO-4, 6%U6d$_\delta$+81%(N,O)2p
HOMO-3, 6%U6d$_\delta$+80%(N,O)2p

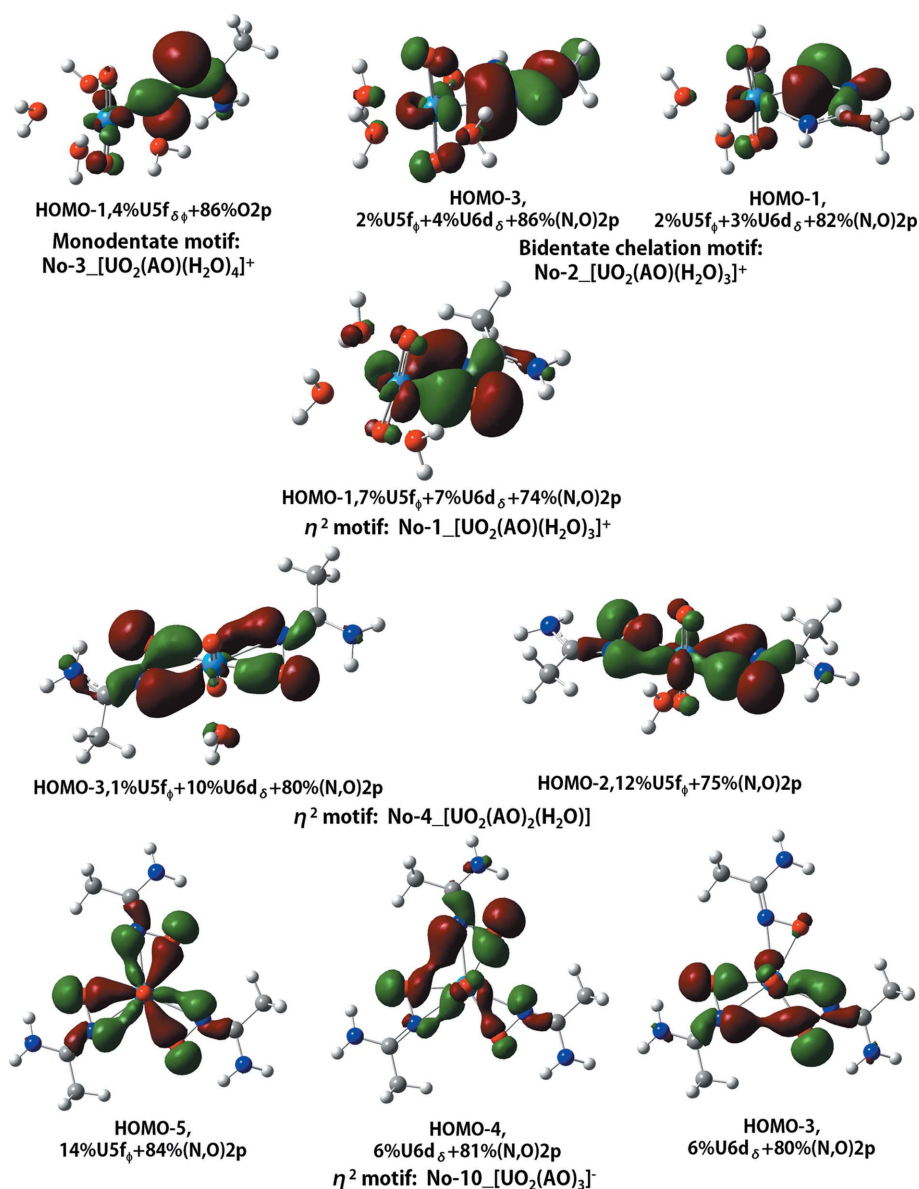**η^2 motif: No-10_[UO_2(AO)$_3$]$^-$**

Figure 6
Main uranyl–AO bonding molecular orbitals and their atomic orbital compositions.

(Xu *et al.*, 2013; Guo, Wang *et al.*, 2015; Guo, Huang *et al.*, 2015). On the basis of the NPA, with the increasing replacement of water molecules by the AO ligands, the natural charges on the uranium atoms decreased, indicating the stronger electron donation from the AO ligand to the uranium than from the water molecule. This observation is also supported by the considerable difference between ΔQ(AO) and ΔQ(H_2O), whose values show AO and H_2O coordination, respectively, transfer ~0.7–0.9 e$^-$ and ~0.2 e$^-$ to uranium.

To further understand the nature of the metal–ligand bonding in uranyl–AO complexes, we performed CDA and some of the relevant uranyl–AO bonding molecular orbitals (MOs) are shown in Fig. 6. The MO plots provide a graphic description of the U—O and U—N σ-bonding, which mainly originates from the interaction of U 5f, 6d orbitals and N, O 2p orbitals. Firstly, we compared the compositions of the MOs involving the metal–ligand bonding in the uranyl–AO complex with different binding motifs, which are significantly different. For the complex No. 3 with a monodentate motif, the U—O σ-bonding MOs contain 4% U 5f$_{\delta\varphi}$ and 86% O 2p character. For model No. 2 with a bidentate chelation motif, HOMO-3 contains 2% U 5f$_\varphi$, 4% U 6d$_\delta$ and 86% (N, O) 2p atomic orbitals and HOMO-1 contains 2% U 5f$_\varphi$, 3% U 6d$_\delta$ and 82% (N, O) 2p character. As for model No. 1 with η^2 motif, the U—O σ-bonding MOs contain 7% U 5f$_\varphi$, 7% U 6d$_\delta$ and 74% N/O character. These results indicate that introduction of the η^2 binding motif increased the uranium 5f orbital character during metal–ligand bonding. To further probe the bonding interaction between uranyl and the AO ligand in uranyl–AO complexes with different AO number, we also performed CDA for compounds No. 4 and No. 10, and present the main uranyl–AO bonding MOs in Fig. 6. Interestingly, the number and shape of MOs associated with the metal–ligand bonding change with the number of coordinated AO ligands. In the UO_2(AO)(H_2O)$_3$$^+$ compound, only one bonding MO between uranyl and AO was found, *i.e.* HOMO-1, which is

composed of 7% U $5f_\varphi$, 7% U $6d_\delta$ and 74% (N, O) $2p$ atomic orbitals. When two AOs coordinated to uranyl ions, in the $UO_2(AO)_2(H_2O)$ compound HOMO-2 and HOMO-3 are formed by the interaction of (N, O) $2p$ with U $5f_\varphi$, $6d_\delta$ orbitals, respectively, while in the $UO_2(AO)_3^-$ compound (Zhang, Su *et al.*, 2016) two MOs, *i.e.* HOMO-3 and HOMO-4, are both composed of 6% U $6d_\delta$ and ~80% (N, O) $2p$ orbitals. In addition, HOMO-5 mainly comes from the interaction of U $5f_\varphi$ and (N, O) $2p$ orbitals. The contributions of U $5f_\varphi$, $6d_\delta$ orbitals to the uranyl–AO bonding MOs obviously increased as the coordinated AO ligands increased, probably because of a better symmetry and energy match with the (N, O) $2p$ orbitals. The strong binding ability of the AO ligand to uranyl is caused by the strong covalent interaction and orbital hybridization between U $5f$, $6d$ and (N, O) $2p$ as shown in Fig. 6.

4. Conclusions

In summary, we explored the geometry and electronic structure of aqueous UO_2^{2+}–amidoxime complex by performing experimental and theoretical analyses of XAFS data combined with DFT calculations. EXAFS fitting in *R* space directly provides information on bond length in the uranyl–amidoxime solution, which then serves as a reference to identify the most probable spatial arrangement of the complex. DFT calculations were performed to simulate the spatial arrangement of the possible binding motif, as well as the bonding nature between the amidoxime ligand and uranyl ions. As a comparison, uranyl contains five water molecules on the equatorial plane and forms a pure hydrate species in uranyl–$HClO_4$ solution. In the highly concentrated amidoxime solution, the hydrate water molecules were replaced by the tris-amidoximate ligands, which coordinate with uranyl ions *via* an η^2 coordination motif. CDA results show that the strong binding ability of the amidoximate ligand to uranyl is caused by the strong covalent interaction and orbital hybridization between U $5f$, $6d$ and (N, O) $2p$. It is worth mentioning that this study provides an approach to directly determine the instinctive coordination properties in uranyl complexes, even in other actinide complexes; this method is particularly suitable in solution systems. In future studies, we will further investigate the detailed coordination geometry structure of the uranyl–amidoximate complex under different environmental conditions (pH, temperature and concentration) using combined diagnostic tools.

References

Abney, C. W., Mayes, R. T., Piechowicz, M., Lin, Z., Bryantsev, V. S., Veith, G. M., Dai, S. & Lin, W. (2016). *Energ. Environ. Sci.* **9**, 448–453.

Andzelm, J., Kölmel, C. & Klamt, A. (1995). *J. Chem. Phys.* **103**, 9312–9320.

Astheimer, L., Schenk, H. J., Witte, E. G. & Schwochau, K. (1983). *Sep. Sci. Technol.* **18**, 307–339.

Bailey, E. H., Mosselmans, J. F. W. & Schofield, P. F. (2005). *Chem. Geol.* **216**, 1–16.

Barber, P. S., Kelley, S. P. & Rogers, R. D. (2012). *RSC Adv.* **2**, 8526–8530.

Barone, V. & Cossi, M. (1998). *J. Phys. Chem. A*, **102**, 1995–2001.

Becke, A. D. (1988). *Phys. Rev. A*, **38**, 3098–3100.

Benfield, R. E., Filipponi, A., Bowron, D. T., Newport, R. J. & Gurman, S. J. (1994). *J. Phys. Condens. Matter*, **6**, 8429–8448.

Cossi, M., Rega, N., Scalmani, G. & Barone, V. (2003). *J. Comput. Chem.* **24**, 669–681.

Dapprich, S. & Frenking, G. (1995). *J. Phys. Chem.* **99**, 9352–9362.

Das, S., Pandey, A. K., Athawale, A. A. & Manchanda, V. K. (2009). *J. Phys. Chem. B*, **113**, 6328–6335.

Davies, R. V., Kennedy, J., McIlroy, R. W., Spence, R. & Hill, K. M. (1964). *Nature (London)*, **203**, 1110–1115.

Di Santo, E., Santos, M., Michelini, M. C., Marçalo, J., Russo, N. & Gibson, J. K. (2011). *J. Am. Chem. Soc.* **133**, 1955–1970.

Dunning, T. H. (1989). *J. Chem. Phys.* **90**, 1007–1023.

Evans, H. T. (1963). *Science*, **141**, 154–158.

Frenking, G. & Fröhlich, N. (2000). *Chem. Rev.* **100**, 717–774.

Frisch, M. J. *et al.* (2009). *Gaussian09.* Gaussian Inc., Wallingford, CT, USA.

Glendening, E. D., Reed, A. E., Carpenter, J. E. & Weinhold, F. (2003). *NBO*, Version 3.1. Gaussian Inc., Pittsburgh, PA, USA.

Gomilšek, J. P., Kodre, A., Arčon, I. & Hribar, M. (2003). *Phys. Rev. A*, **68**, 042505.

Gückel, K., Tsushima, S. & Foerstendorf, H. (2013). *Dalton Trans.* **42**, 10172–10178.

Guo, X., Huang, L., Li, C., Hu, J., Wu, G. & Huai, P. (2015). *Phys. Chem. Chem. Phys.* **17**, 14662–14673.

Guo, X., Wang, Y., Li, C., Huai, P. & Wu, G. (2015). *Mol. Phys.* **113**, 1327–1336.

Hennig, C. (2007). *Phys. Rev. B*, **75**, 035120.

Hennig, C., Schmeide, K., Brendler, V., Moll, H., Tsushima, S. & Scheinost, A. C. (2007). *Inorg. Chem.* **46**, 5882–5892.

Ikeda-Ohno, A., Hennig, C., Rossberg, A., Funke, H., Scheinost, A. C., Bernhard, G. & Yaita, T. (2008). *Inorg. Chem.* **47**, 8294–8305.

Ikeda-Ohno, A., Hennig, C., Tsushima, S., Scheinost, A. C., Bernhard, G. & Yaita, T. (2009). *Inorg. Chem.* **48**, 7201–7210.

Jackson, V. E., Gutowski, K. E. & Dixon, D. A. (2013). *J. Phys. Chem. A*, **117**, 8939–8957.

Katragadda, S., Gesser, H. D. & Chow, A. (1997). *Talanta*, **45**, 257–263.

Kim, J., Tsouris, C., Mayes, R. T., Oyola, Y., Saito, T., Janke, C. J., Dai, S., Schneider, E. & Sachde, D. (2013). *Sep. Sci. Technol.* **48**, 367–387.

Kim, J., Tsouris, C., Oyola, Y., Janke, C. J., Mayes, R. T., Dai, S., Gill, G., Kuo, L.-J., Wood, J., Choe, K.-Y., Schneider, E. & Lindner, H. (2014). *Ind. Eng. Chem. Res.* **53**, 6076–6083.

Klamt, A. & Schüürmann, G. (1993). *J. Chem. Soc. Perkin Trans. 2*, pp. 799–805.

Kodre, A., Arcon, I., Gomilsek, J. P., Preseren, R. & Frahm, R. (2002). *J. Phys. B*, **35**, 3497–3513.

Lee, C., Yang, W. & Parr, R. G. (1988). *Phys. Rev. B*, **37**, 785–789.

Liu, Q., Zhang, Q., Yang, S., Zhu, H., Liu, Q. & Tian, G. (2017). *Dalton Trans.* **46**, 13180–13187.

Lu, T. & Chen, F. (2012). *J. Comput. Chem.* **33**, 580–592.

McGrail, B. T., Sigmon, G. E., Jouffret, L. J., Andrews, C. R. & Burns, P. C. (2014). *Inorg. Chem.* **53**, 1562–1569.

Neuefeind, J., Soderholm, L. & Skanthakumar, S. (2004). *J. Phys. Chem. A*, **108**, 2733–2739.

Ravel, B. & Newville, M. (2005). *J. Synchrotron Rad.* **12**, 537–541.

Rehr, J. J., Kas, J. J., Vila, F. D., Prange, M. P. & Jorissen, K. (2010). *Phys. Chem. Chem. Phys.* **12**, 5503–5513.

Schenk, H. J., Astheimer, L., Witte, E. G. & Schwochau, K. (1982). *Sep. Sci. Technol.* **17**, 1293–1308.

Seko, N., Katakai, A., Tamada, M., Sugo, T. & Yoshii, F. (2004). *Sep. Sci. Technol.* **39**, 3753–3767.

Sémon, L., Boehme, C., Billard, I., Hennig, C., Lützenkirchen, K., Reich, T., Rossberg, A., Rossini, I. & Wipff, G. (2001). *ChemPhysChem*, **2**, 591–598.

Ting, C. F., Jie, X., Wei, H. J., Mei, G., Sheng, H. & Lin, W. X. (2013). *J. Dispersion Sci. Technol.* **34**, 604–610.

Vetere, V., Maldivi, P. & Adamo, C. (2003). *J. Comput. Chem.* **24**, 850–858.

Vukovic, S. & Hay, B. P. (2013). *Inorg. Chem.* **52**, 7805–7810.

Vukovic, S., Watson, L. A., Kang, S. O., Custelcean, R. & Hay, B. P. (2012). *Inorg. Chem.* **51**, 3855–3859.

Wang, C.-Z., Lan, J.-H., Wu, Q.-Y., Luo, Q., Zhao, Y.-L., Wang, X.-K., Chai, Z.-F. & Shi, W.-Q. (2014). *Inorg. Chem.* **53**, 9466–9476.

Weinhold, F. & Landis, C. R. (2005). *Valency and Bonding: a Natural Bond Orbital Donor–Acceptor Perspective.* Cambridge University Press.

Witte, E. G., Schwochau, K. S., Henkel, G. & Krebs, B. (1984). *Inorg. Chim. Acta*, **94**, 323–331.

Xu, C., Su, J., Xu, X. & Li, J. (2013). *Sci. China Chem.* **56**, 1525–1532.

Zhang, L., Su, J., Yang, S., Guo, X., Jia, Y., Chen, N., Zhou, J., Zhang, S., Wang, S., Li, J., Li, J., Wu, G. & Wang, J.-Q. (2016). *Ind. Eng. Chem. Res.* **55**, 4224–4230.

Zhang, A., Uchiyama, G. & Asakura, T. (2005). *React. Funct. Polym.* **63**, 143–153.

Zhang, L., Zhou, J., Zhang, J., Su, J., Zhang, S., Chen, N., Jia, Y., Li, J., Wang, Y. & Wang, J.-Q. (2016). *J. Synchrotron Rad.* **23**, 758–768.